Microtomographic assessment of damage in P91 and E911 steels after long-term creep

Loïc Renversade[a], Herbert Ruoff[b], Karl Maile[b], Federico Sket[c], András Borbély[a]

[a] Ecole Nationale Supérieure des Mines, SMS-EMSE, CNRS:UMR 5307, LGF, Saint-Etienne, France
[b] Materialprüfungsanstalt Universität Stuttgart (MPA), Stuttgart, Germany
[c] Madrid Institute for Advanced Studies of Materials (IMDEA Materials Institute), Madrid, Spain

Two flat hollow cylinders made of martensitic 9 wt.% Cr steels were creep deformed under in-service conditions typical of steam pipes at fossil-fuel fired power plants. Damage in the tubes was assessed through synchrotron X-ray microtomography by evaluating the shape, size and spatial-distribution of voids. The analysis of the size distribution of non-coalesced voids suggested that void growth is controlled by the plasticity constrained diffusional mechanism, a hypothesis verified by micromechanical simulations. A much higher void density was found in steel grade P91 compared to E911.

Keywords: Chromium steel; Creep damage; Microtomography; Modeling; Void growth

1. Introduction

Thanks to their good creep and creep-damage resistance ASTM steel grades P91 and E911 are currently in use as components of ultra supercritical power plants of high efficiency [1]. Creep resistance is usually achieved by alloying with several elements (Cr, Mo, W, V, Nb) and by a complex multiphase-structure obtained through austenitizing and tempering heat treatments. Controlling damage resistance is less obvious. For example, second phase particles located at grain boundaries usually retard the recovery of the microstructure, which is beneficial for creep resistance, but the same particles are often nucleation sites of voids [2] leading to fracture. Since void nucleation takes place at the nanometer scale less knowledge exists about this mechanism, especially when the formation of the second phase particles/precipitates takes place during creep as in the case of the present studies. It is mostly accepted that structural changes accelerate creep and intergranular damage, but the general validity of this statement is still an open question, each specific case requiring adequate investigations.

Creep damage is a highly complex phenomenon involving the superposition of nucleation, growth and coalescence of voids. As has been pointed out [3] understanding the factors governing these phenomena requires studying them independently. Growth for example was related to the size of the largest [3] or to the i^{th} largest void [4] and not to the mean size, which is inherently influenced by continuous nucleation. The subject has been widely treated theoretically [2], while its experimental assessment was rendered difficult by several factors [2–4]. For instance conventional metallography – inherently delivering two dimensional information – may give biased results due to artifacts introduced during sample preparation [5]. Serial sectioning allows reconstructing three dimensional (3D) structures and the measurement of real 3D quantities such as void volume, void-to-void distance and grain boundary angles [6], but the technique remains limited to relatively small volumes due to the extreme amount of manual intervention necessary to merge the structural information of different sections. Recently, synchrotron X-ray microtomography (SXRM) [7, 8] has proven to be an excellent method for characterizing creep damage not only in 3D [5, 7–11], but also as a function of time [12–14]. Its advantage over serial sectioning resides in its nondestructive nature and

the larger field of view allowing meaningful statistical evaluations. It is the aim of the present work to apply the SXRM technique to damage assessment in two hollow cylinders made of P91 and E911 steels subjected to long-term creep.

2. Experimental

Creep tests were performed on two flat hollow cylinders (Fig. 1) made of P91 (9–1 %CrMoVNb) and E911 (9–1-1 %CrMoWVNb) martensitic steels having the chemical compositions shown in Table 1. The main difference between them is related to the extra 1 wt.% of W present in E911, which initially is in solid-solution, but with time stabilizes the $M_{23}C_6$ carbides and precipitates at grain boundaries as Fe_2W Laves phase [15, 16]. The samples were subjected to multi-axial loads characteristic of steam pipes under in-service conditions. The loads are given in Table 2 and consist of: internal pressure (applied by means of nitrogen gas inside the cylinder), axial tensile load and high temperature which is slightly different for P91 and E911 steels (575 °C and 600 °C, respectively). Creep was interrupted after 10 200 h and 37 800 h (tertiary creep regime) for specimens made of P91 and E911 steels, respectively. Small cylindrical samples of 0.6 mm in diameter and 2.5 mm in length (along the radius of the cylinder) were extracted for SXRM investigations from the mid-length of the tubes (Fig. 1). Microtomography was performed at beam line ID19 of the European Synchrotron Radiation Facility using X-rays with energy of 52 keV. The radiograms were measured with an X-ray detector including a YAG:Ce scintillator, visible light optics and a CCD camera. The detector had an effective pixel size of 0.28 μm and a field of view of about 0.6 mm × 0.6 mm. The whole sample length of 2.5 mm had to be scanned therefore in five adjacent subvolumes (with some overlap), which were later merged using image correlation. Creep voids were identified and extracted from reconstructions using a gradient based local threshold combined with the watershed algorithm [17]. Only voids having a volume larger than 125 voxels (approximately 2 μm^3) were analyzed. This lower limit was selected in agreement with literature data indicating that the shape and volume of an ellipsoid can be already well approximated by a structure of 125 voxels [18]. Furthermore, void shape was characterized in terms of two parameters: the complexity factor *CF* and the elongation *e* as defined in Ref. [9]. The *CF* is related to the difference in shape between the real cavity and its equivalent ellipsoid having identical volume and moment of inertia. It is defined as the ratio between the sum of the relative complement (set-theoretic difference) of the cavity in the ellipsoid and of the ellipsoid in the cavity (when their center of mass coincides) over the void volume. The elongation (*e*) corresponds to the ratio between the major semi-axis and the mean of the intermediate and minor semi-axes of the equivalent ellipsoid. Applying visually determined threshold levels for *CF* ($CF < 0.5$) and *e* ($e < 1.9$) the non-coalesced voids could be identified. The histogram of the equivalent radii (the diameter of a sphere of identical volume) was analyzed based on a general theory accounting for the nucleation and growth of the voids [2]. Choosing different threshold levels around $CF = 0.5$ and $e = 1.9$ influenced only slightly the experimental histogram and the parameters describing it. The total void population comprising the coalesced and non-coalesced voids was expressed only in terms of void density N_V, defined as the number of voids per unit volume.

3. Results

3.1. Experimental results

Figure 2a and b shows typical metallographic images of the P91 and E911 steel, respectively. Their microstructure consists of tempered martensite, but primary austenite grains are also visible. The average grain size is of about two times larger in the E911 specimen (31 μm) compared to P91

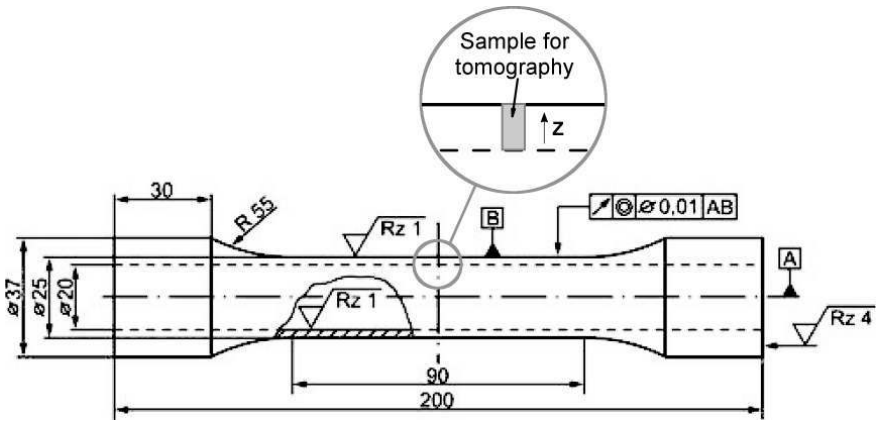

Fig. 1. Geometry of the creep-deformed flat hollow cylinders. The insert shows the sample extracted for tomographic measurements.

Table 1. Chemical composition of the P91 and E911 steels (wt.%) (Fe balance).

Grade	C	Si	Mn	P	S	Cr	Ni	Al	Nb	Mo	V	W
P91	0.09	0.33	0.41	0.011	0.002	8.59	0.26	0.016	0.072	0.93	0.20	–
E911	0.11	0.18	0.46	0.015	0.003	8.61	0.21	0.013	0.089	0.92	0.19	0.995

Table 2. Creep testing conditions: temperature (T), axial stress (σ_a), internal pressure (p), creep time (t) and minimum strain-rate ($\dot{\varepsilon}_{min}$).

Material	T (°C)	σ_a (MPa)	p (MPa)	t (h)	$\dot{\varepsilon}_{min}$ (s^{-1})
P91	575	52.6	23.6	10200	1×10^{-10}
E911	600	48.9	17.7	37800	5×10^{-11}

(15.6 μm). Most of the voids are aligned along the martensite laths, which in turn seem to be uniformly distributed on the set of all possible orientations. It is visually evident that voids are larger in E911 steel than in P91, while the opposite is true for the void density. Similar qualitative results were obtained from tomographic reconstructions too (Fig. 3a), which indicate in addition the spatial distribution of voids in the tube wall. The quantitative void density data shown in Fig. 3b emphasize that there are fewer voids near the inner surface of the tube than in the outer region. Each point on the graph corresponds to the number of voids (coalesced or not) found in a cylindrical slab of 25 μm in height (of about 100 voxels) and a diameter equal to that of the tomographic sample (0.6 mm). The two samples show significantly different distributions. Remarkable is the steep increase of N_V in the P91 steel (at $Z \approx 0.5$ mm), a feature which is not observed in E911 and where N_V increases only slightly from the inner towards the outer surface of the tube. The maximum N_V is found close to the wall's outer surface for both samples, but it is about 6 times higher in the P91 (180000 mm^{-3}) than in the E911 steel (30000 mm^{-3}).

Non-coalesced voids were analyzed in terms of their size distribution. According to Fig. 4 there is a considerable difference between the distributions of void diameters in the two steels. The mean values are of about 2 μm and 4.5 μm P91 and E911, respectively. The larger value found for E911 is also related to a wider distribution. A theoretically derived function taking into account nucleation and growth of voids was used to evaluate the experimentally obtained histograms [2]:

$$N(R,t) = \frac{A_2}{A_1} R^{\beta} t^{1+\gamma} \exp\left(-\frac{1+\gamma}{1+\beta}\frac{R^{\beta+1}}{A_1}\right) \quad (1)$$

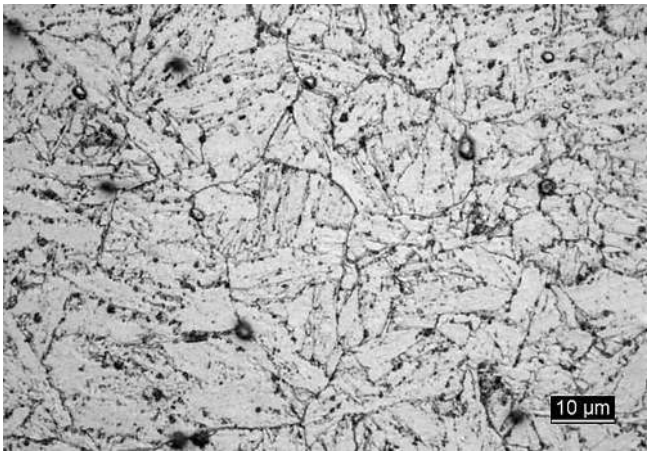

(a)

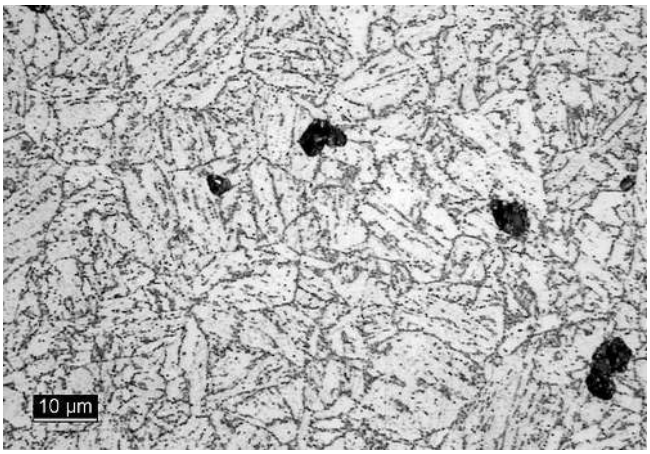

(b)

Fig. 2. Optical micrograph of (a) the P91 steel after 10200 h and of (b) the E911 steel after 37800 h of creep showing a martensitic microstructure with voids aligned along the martensite laths.

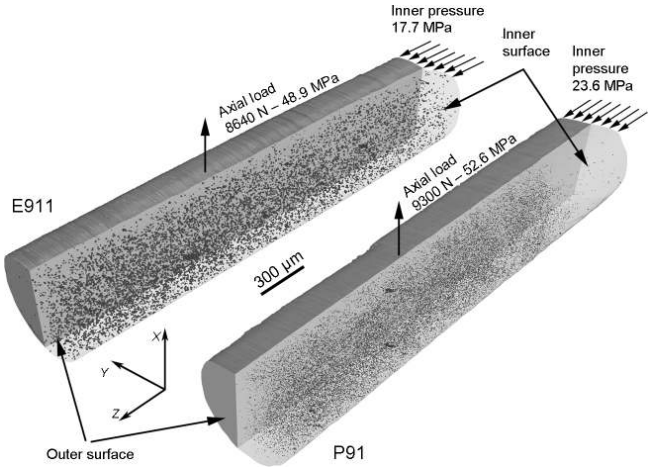

(a)

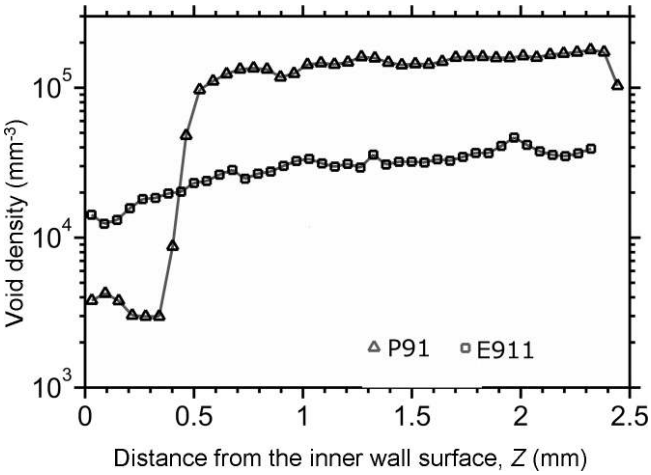

(b)

Fig. 3. Damage distribution in E911 and P91 steels: (a) tomographic reconstruction of damage after 37800 and 10200 h, respectively. (b) Void density of all cavities through the wall thickness (indicated by the Z-axis, which has the origin at the inner surface of the tube).

where $N(R,t)$ represents the number of voids with radii between R and $R + dR$ in the time interval t and $t + dt$. The unknown constants A_1 and β are related to the non-stationary growth rate of the void radius

$$\dot{R} = A_1 R^{-\beta} t^{-1} \tag{2}$$

while A_2 and γ to the nucleation rate [2]:

$$J = A_2 t^{\gamma} \tag{3}$$

The physical significance of A_1 and A_2 are usually given by the void-growth and nucleation-rate models [2]. They may depend on the stress state or other deformation conditions, but not on the time t or cavity radius R. Since the experimentally obtained size distribution was estimated for constant time t, only the determination of the exponent β, is possible. Therefore, the parameters A_1, A_2 and γ will not be discussed. Similarly to previous literature results on a notched hollow cylinder made of E911 steel [5], Eq. (1) fits the present experimental data (Fig. 4) relatively well and in spite of their very different broadening both distributions are described by nearly identical values of $\beta \approx 2.1 \pm 0.3$.

It is known from the literature [2, 19, 20] that $\beta = 2$ is characteristic for the constrained diffusional mechanism of void growth, a hypothesis that can be verified by simulations. To do this, we have assumed according to Ref. [3] that the largest non-coalesced voids found in tomographic reconstructions have nucleated at the beginning of the creep test. As their size is not affected by continuous nucleation it becomes possible comparing experimental and simulated cavity sizes and to draw conclusions about the supposed growth mechanism. Thanks to the large analyzed sample of 2.5 mm in length it was also possible to link the size of the largest non-coalesced voids to their position along the tube wall. The points shown in Fig. 5 correspond to the largest non-coalesced void diameter found in cylindrical subvolumes with a height of 125 μm along the tube radius. Again a marked difference between the two steels was found. The largest void diameters are varying in the range of 5.7 ± 1.3 μm and 9.2 ± 2.8 μm for the P91 and E911 samples, respectively. The results show, however, a significant scatter that should be related to the fact that each measurement point corresponds to one single void. Figure 5 also shows some of these largest cavities, whose shape is not perfectly ellipsoidal. Some voids in E911 steel have short branches, suggesting that they are positioned at triple junctions or at quadruple points.

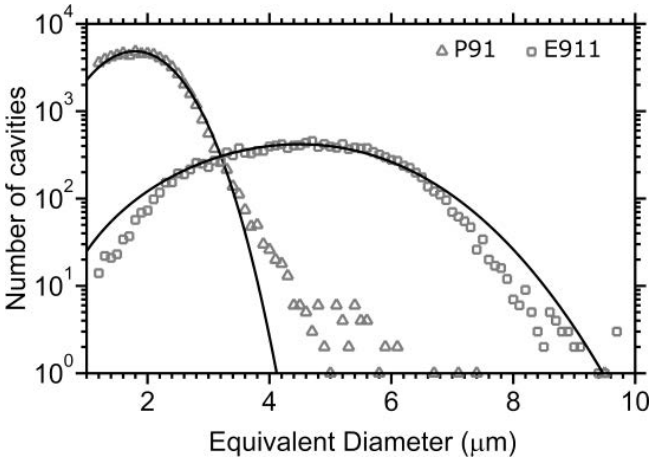

Fig. 4. Size distribution of non-coalesced voids in P91 and E911 steels. The continuous lines represent the fit of Eq. (1).

3.2. Simulation results of void growth

Based on the experimentally obtained value of β close to 2, void growth was simulated according to the constrained diffusional mechanism predicting the following growth-rate of the void radius R [2]:

$$\dot{R} = \frac{\sigma_{\mathrm{I}}^{\infty} - (1-\omega)\sigma_0}{\left[\dfrac{k_{\mathrm{B}}T}{\Omega\delta D_{\mathrm{b}}} + \dfrac{\pi^2(1+3/n)^{1/2}}{\lambda^2 g}\dfrac{\sigma_{\mathrm{e}}^{\infty}}{\dot{\varepsilon}_{\mathrm{e}}^{\infty}}\right]R^2} \tag{4}$$

where k_{B} is the Boltzmann constant, T the temperature, n the stress exponent, Ω the atomic volume and δD_{b} is the product of the grain boundary width δ and the grain boundary diffusion coefficient D_{b}. The mean grain size g and the mean inter-void spacing λ were evaluated from metallographic sections and tomographic reconstructions, respectively. They are given in Table 3 together with other material parameters taken from the literature [16, 21]. In simulations the product of the sintering stress σ_0 and the fraction of non-cavitated grain boundaries $(1-\omega)$ was ne-

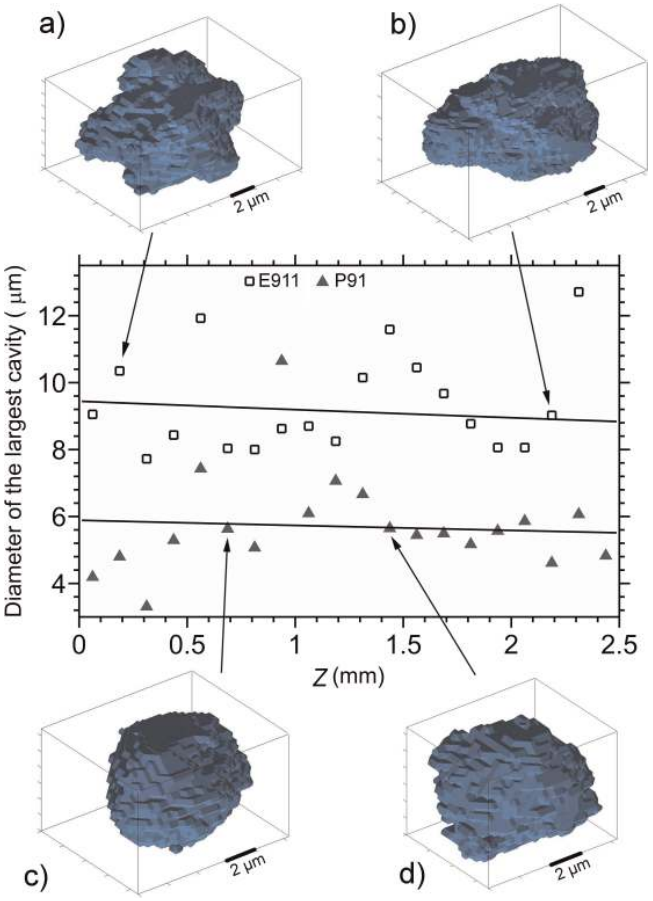

Fig. 5. Variation of the largest non-coalesced void diameter through the wall thickness of the hollow cylinder. Experimental data from tomography (symbols) and results of micromechanical simulations (continuous lines) are compared. Typical voids are also shown.

Table 3. Material and microstructural parameters of creep specimens: grain boundary width δ, times the grain boundary diffusion coefficient (δD_b) [21], stress-exponent (n) [16], Young's modulus (E), Poisson's ratio (ν), grain size (g), nearest-neighbor distance (λ) and the average diameter of the largest non-coalesced voids (D_{max}).

Material	δD_b ($m^3 s^{-1}$)	n	E (GPa)	ν	g (μm)	λ (μm)	D_{max} (μm)
P91	5×10^{-21}	6	175	0.3	15.6	10.8	5.7 ± 1.3
E911	1×10^{-20}	6	175	0.3	31	16.5	9.2 ± 2.8

glected beside σ_I^∞, which is the component of the applied stress normal to the grain boundary. Since the actual stress state is triaxial, σ_I^∞ was considered equal to the maximum principal stress (*MPS*) and was obtained from finite element (FE) simulations describing the creep deformation of the tubes. The FE simulation was done with the commercial software ABAQUS using axisymmetric elements and a viscoplastic Norton law [20]. The unknown parameters of the Norton law were adjusted until the calculated axial creep curves agreed well with the experimental ones. As the chemical composition of the two steels is just slightly different and the testing temperatures differ only by 25 K identical elastic constants were considered for both materials (Table 3).

The results of FE simulations indicate that both *MPS* and von Mises stress (*VMS*) vary along the cylinder wall and as a function of time (Fig. 6). Two curves are drawn for each stress quantity, one characteristic for the beginning of the test and one for the time when the deformation was stopped. The average *MPS* and *VMS* values (for one sample) are not very different, but they have different monotonic behavior: the *MPS* increases, while the *VMS* decreases towards the tube's outer surface. The *MPS* is mainly influenced by the hoop stress-component (increasing with tube radius), while the *VMS* by the radial component. The latter is equal to the internal pressure at the inner surface and decreases to zero at the outer surface of the tube. Both *MPS* and *VMS* show

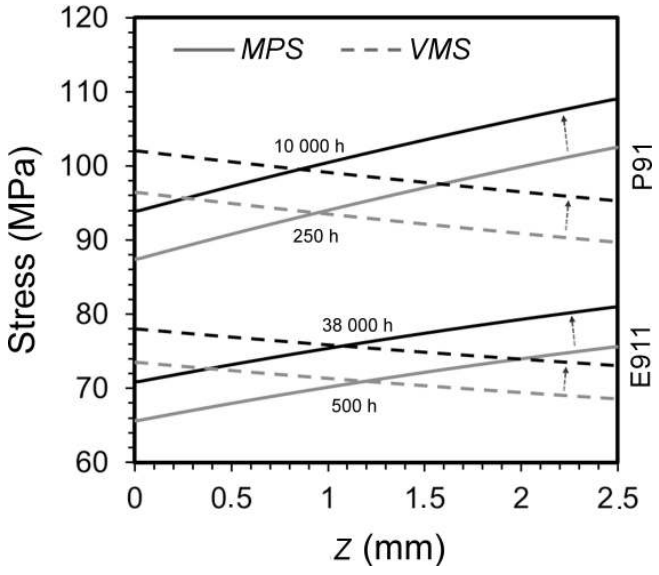

Fig. 6. Maximum principal stress (*MPS*) and von Mises stress (*VMS*) through the tube wall as obtained from FE simulations. Each stress quantity is described by two curves, one at the beginning and one at the end of the test.

a small increase (7 %) with creep time. Due to the slightly higher applied loads the *MPS* and *VMS* are both higher in the P91 specimen compared to E911. The final void radius was calculated by integrating Eq. (4) over the duration of the creep test from an initial radius at nucleation of 5 nm. Considering a lower critical value did not significantly affect the final void size. Taking into account the local stress histories the variation of the maximum void size through the tube wall was also predicted. The results are plotted as continuous lines in Fig. 5. The mean values over the tube wall at the end of the tests are of about 5.7 μm and 9.1 μm for P91 and E911 steel, respectively.

4. Discussion

An important aspect of the present damage analysis concerns the representativeness of the results. This issue applies, however, to the many microtomography investigations since the field of view of the utilized detectors is only 3 orders of magnitude larger than the pixel size. To cope with this problem 5 adjacent volumes were scanned in this work, but even in this case the size of the analyzed tomographic sample (Fig. 1) was much smaller than the creep deformed tube. In order to conclude about the representativeness of the presented results two conditions related to the microstructure of the specimens should be analyzed. These are the statistical homogeneity of the i) grain and ii) void structure at the length-scale of the analyzed volumes. This assures that by randomly selecting small volumes (equal to that of the scanned sample) at different locations of the tube, the distributions of the grain and void sizes, respectively will coincide. Considering the average grain sizes (Table 3) it can be estimated that there are at least 30 000 and 260 000 grains in the analyzed volume of the E911 and P91 steel, respectively. Such a high number of grains assures, very probably, the representativeness of the grain size distribution as well as the co-related distribution of the possible void nucleation sites.

The second condition concerning the statistical homogeneity of the void structure is more restrictive, since it limits the tomography analysis to samples free of macroscopic heterogeneities with size comparable to that of the scanned volumes. This also means that void size distribution obtained on specimens originating from broken samples is not representative since a huge heterogeneity (crack) was already present at a different location in the tube. Moreover, the presence of a macroscopic crack in the tube leads to additional local interaction effects such as plastic localization, which accelerates local damage and leads to significant damage gradients [22]. In the present case both creep tests were interrupted well before fracture and accordingly the largest void diameters, identified as the major axis of their

equivalent ellipsoid, were much smaller (53 μm and 36 μm for the P91 and E911 samples, respectively) than the smallest linear dimension of the analyzed specimens (of about 600 μm). Furthermore, the exponent $\beta \cong 2$ was obtained from the size distribution of a large number (17 877 and 41 426 for E911 and P91, respectively) of non-coalesced voids, which should assure the representativeness of this result.

The void size predicted on the basis of Eq. (4) is in reasonable agreement with experimental data (Fig. 5) indicating that the model of constrained diffusional growth is a good approximation for predicting void growth in P91 and E911 steels. The model allows, however, a much finer analysis of damage distribution in the tube predicting for example a monotonic decrease in the largest void size towards the outer surface of the wall. This change is, however, small rendering difficult an experimental verification due to the large scatter of the original data. Another interesting point is related to the structure of Eq. (4). It was found numerically that under the conditions of the present experiments the contribution of the diffusional term in the denominator is negligible with respect to the plastic term, which being the slower mechanism will finally control void growth. Assuming equality between the diffusional and plastic terms, a limiting strain-rate defining the border between pure diffusional and constrained growth can be derived. Under the conditions of the present tests this limit strain-rate is of the order of 10^{-6} s^{-1} (for both specimens), which compared to experimental values (Table 2) indicates the presence of the constrained mechanism. Simulations also indicated that the diffusion coefficient may vary by three orders of magnitude without any significant influence on the predicted void size.

Stopping the calculations for E911 steel after 10 000 h (corresponding to the creep time of the P91 specimen) the average cavity diameter was 5.8 μm, close to the mean value of 5.7 μm observed in the P91 specimen. This indicates that creep time is the major experimental parameter responsible for the void-size difference in the two samples and that the real void growth-rates are well captured by the model. This indirectly implies that microstructural differences like stabilized $M_{23}C_6$ carbides and Laves phases do not influence void growth up to the creep exposure time considered in this study.

The other significant difference between the two specimens concerns void density (Fig. 3b), which should be related to processes of nucleation and coalescence. Based on the different grain sizes (g) and next-neighbor distances (λ) of the two specimens (Table 2) it can concluded that coalescence is less frequent in E911 than in P91 as both parameters are larger in the former. This statement was independently checked using void shape analysis made possible by the high-resolution 3D tomographic reconstructions of the voids. The visually selected threshold values for the complexity factor CF, and elongation e, indicate that only 16 % (2 857 out of 17 877) of voids have complex shape in the E911 sample, while this ratio increases to 43 % (17 673 out of 41 426) for P91. Evidently, the larger void density in P91 steel should be mainly linked to the void nucleation propensity of the material. Since voids are located at grain boundaries the predisposition of a material to void nucleation is described by the number of voids per unit grain-boundary area N_s. This can be obtained dividing N_V by the specific boundary surface S_V, which owing to the smaller grain size is of about two times larger in P91 compared to E911. Considering the ratio of the maximum void-densities (of about 6) of the two steels we conclude that N_s is at least 3 times higher in P91 than in E911. Obviously, the difference is related to the different microstructures of the steels. It is well known that the newer steel grade E911 has better creep properties than P91 [16] which is usually attributed to the extra 1 wt.% of W. At the beginning of creep W is in solid solution in the matrix, with time however, it precipitates into the intermetallic Laves phase (Fe_2W) and stabilizes the $M_{23}C_6$ carbides present at grain boundaries [15, 16]. This slows down the recovery of the martensite and implicitly increases the creep strength. From the point of view of damage, one may argue that the stabilized carbides and Fe_2W present at grain boundaries can prevent grain boundary sliding, known as a possible void nucleation mechanism at low stresses [2, 20]. Therefore, in the context of the present comparison we suggest that the extra 1 wt.% of W significantly reduces the cavity nucleation-rate in E911 steel compared to P91.

Void density at the length scale of the tube wall is more homogeneously distributed in E911 than in P91 steel. The remarkable increase in N_V at 0.5 mm from the tube's inner surface (Fig. 3b), however, is not only characteristic for the P91 steel, but it was also observed in E911 [23]. The applied stresses in the latter case were, however, smaller (inner pressure of 14 MPa, axial stress of 38.7 MPa) compared to the case of the E911 specimen investigated here. This abrupt change in N_V suggests that void nucleation might be driven by the maximum principal stress, the maximum value of which moves with time from the outer tube surface towards the interior. Nevertheless, at this state of the analysis it is premature drawing any conclusions, the supposition requiring systematic studies.

Present analysis is essentially based on the 3D high-resolution information obtained by SXRM, which allowed identifying the presence of the constrained growth-mechanism based on the size-distribution of non-coalesced voids. The technique becomes, however, limited if information on void position with regard to grain boundaries is needed. Combining microtomography with serial sectioning, Gupta et al. [11] have recently shown that damage in creep-deformed tempered martensitic steels with slightly different chemical composition (10.86 wt.% Cr and 3 wt.% Co) is preferentially located at prior austenite grain boundaries. This shows the extra power of the combination of different complementary techniques, which can be very beneficial for creep damage studies.

5. Conclusion

Two hollow cylinders made of martensitic P91 and E911 steels were creep deformed under service conditions characteristic of steam pipes at fossil-fuel fired power plant. Creep damage was characterized using synchrotron microtomography in terms of shape, size and spatial-distribution of voids. For both steels, the size-distribution of non-coalesced voids could be satisfactorily fitted by a general function (Eq. (1)) accounting for continuous void nucleation and growth. The exponent β characterizing the growth rate of void radius was found to be close to 2, suggesting that

cavity growth is controlled by the constrained diffusional mechanism. This prediction was verified by numerical simulations, which led to a satisfactory agreement between the predicted and measured size of the largest non-coalesced voids.

Void nucleation is less probable in the E911 material, corroborating the assumption that the extra 1 wt.% of W makes an additional contribution to the stabilization of grain boundaries (by stabilizing the $M_{23}C_6$ carbides and precipitating the Fe_2W Laves phase) and thus retarding grain boundary sliding and consequently void nucleation.

The authors acknowledge Elodie Boller beamline staff at ID-19 (ESRF) for her help during measurements.

References

[1] F. Abe, T.-U. Kern, R. Viswanathan (Eds.): Creep-resistant steels, Woodhead Cambridge (2008). DOI:10.1533/9781845694012
[2] H. Riedel: Fracture at High Temperature, Springer-Verlag, Berlin (1987). DOI:10.1007/978-3-642-82961-1
[3] B.J. Cane, G.W. Greenwood: Met. Sci. 9 (1975) 55. DOI:10.1179/030634575790444405
[4] N.G. Needham, T. Gladman: Met. Sci. 14 (1980) 64. DOI:10.1179/030634580790426300
[5] F. Sket, K. Dzieciol, A. Borbély, A.R. Kaysser-Pyzalla, K. Maile, R. Scheck: Mater. Sci. Eng. A 528 (2010) 103. DOI:10.1016/j.msea.2010.07.029
[6] A.A. Wahab, M.V. Kral: Mater. High Temp. 24 (2007) 299. DOI:10.1179/096034007X267781
[7] J. Banhart, A. Borbély, K. Dzieciol, F. Garcia-Moreno, I. Manke, N. Kardjilov, A.R. Kaysser-Pyzalla, M. Strobl, W. Treimer: Int. J. Mater. Res. 101 (2010) 9. DOI:10.3139/146.110382
[8] C. Redenbach, A. Rack, K. Schladitz, O. Wirjadi, M. Godehardt: Int. J. Mater. Res. 103 (2012) 217. DOI:10.3139/146.110671
[9] A. Isaac, F. Sket, W. Reimers, B. Camin, G. Sauthoff, A.R. Pyzalla: Mater. Sci. Eng. A 476 (2008) 108. DOI:10.1016/j.msea.2007.05.108
[10] K.S. Cheong, K.J. Stevens, Y. Suzuki, K. Uesugi, A. Takeuchi: Mater. Sci. Eng. A 513–514 (2009) 222.
[11] C. Gupta, H. Toda, C. Schlacher, Y. Adachi, P. Mayr, C. Sommitsch, K. Uesugi, Y. Suzuki, A. Takeuchi, M. Kobayashi: Mater. Sci. Eng. A 564 (2013) 525. DOI:10.1016/j.msea.2012.12.002
[12] A.R. Pyzalla, B. Camin, T. Buslaps, M. Di Michiel, H. Kaminski, A. Kottar, A. Pernack, W. Reimers: Science 308 (2005) 92. DOI:10.1126/science.1106778
[13] K. Dzieciol, A. Borbély, F. Sket, A. Isaac, M. Di Michiel, P. Cloetens, T. Buslaps, A.R. Pyzalla: Acta Mater. 59 (2011) 671. DOI:10.1016/j.actamat.2010.10.003
[14] A. Isaac, K. Dzieciol, F. Sket, A. Borbély: Metall. Mater. Trans. A 42 (2011) 3022. DOI:10.1007/s11661-011-0781-1
[15] F. Abe, S. Nakazawa: Metall. Trans. A 23 (1992) 3025. DOI:10.1007/BF02646120
[16] A. Czyrska-Filemonowicz, A. Zielińska, P.J. Ennis: J. Achiev. Mater. Manuf. Eng. 19 (2006) 43.
[17] K. Dzieciol, A. Borbély, M. Scheel: J. Physics: Conference Series 425 (2013) 192005. DOI:10.1088/1742–6596/425/19/192005
[18] E.J. Garboczi: Cem. Concr. Res. 32 (2002) 1621. DOI:10.1016/S0008-8846(02)00836-0
[19] B.F. Dyson: Scr. Metall. 17 (1983) 31. DOI:10.1016/0036-9748(83)90065-0
[20] M.E. Kassner, M.T. Perez-Prado: Fundamentals of Creep in Metals and Alloys, Elsevier (2004).
[21] Y. Lijima: J. Phase Equilib. Diff. 26 (2005) 466. DOI:10.1007/s11669-005-0036-1
[22] R. Abbasi, L. Renversade, K. Dzieciol, A. Borbély, A.R. Kaysser-Pyzalla: Int. J. Mater. Res. 103 (2012) 228. DOI:10.3139/146.110662
[23] F. Sket, K. Maile, H. Ruoff, R. Scheck, A. Borbély: Proc. 12th Int. Conf. on Creep and Fracture of Engineering Materials and Structures, The Japan Institute of Metals (2012), paper 228.

Correspondence address

Prof. András Borbély
158 cours Fauriel
4200 Saint-Etienne
France
Tel.: +33 477 42 02 79
Fax: +33 477 42 00 01
E-mail: borbely@emse.fr